Structural Characterization of the Ribosomal P1A−P2B Protein Dimer by Small-Angle X-ray Scattering and NMR Spectroscopy†

Przemysław Grela,[‡,§] Magnus Helgstrand,[§,||] Dawid Krokowski,[‡] Aleksandra Boguszewska,[‡] Dmitri Svergun,[⊥] Anders Liljas,[@] Pau Bernadó,[#] Nikodem Grankowski,[‡] Mikael Akke,*[,||] and Marek Tchórzewski*[,‡]

Department of Molecular Biology, Institute of Microbiology and Biotechnology, Maria Curie-Skłdowska University, Akademicka 19, 20-033 Lublin, Poland, Department of Biophysical Chemistry, Lund University, P.O. Box 124, SE-221 00 Lund, Sweden, European Molecular Biology Laboratory, Hamburg Outstation, Notkestrasse 85, 22603 Hamburg, Germany, Institute of Crystallography, Russian Academy of Sciences, Leninsky pr. 59, 117333 Moscow, Russia, Department of Molecular Biophysics, Lund University, P.O. Box 124, SE-221 00 Lund, Sweden, and Institut de Recerca Biomèdica, Parc Científic de Barcelona, Josep Samitier 1-5, 08028 Barcelona, Spain

Received August 14, 2006; Revised Manuscript Received November 15, 2006

ABSTRACT: The five ribosomal P-proteins, denoted P0-$(P1-P2)_2$, constitute the stalk structure of the large subunit of eukaryotic ribosomes. In the yeast *Saccharomyces cerevisiae*, the group of P1 and P2 proteins is differentiated into subgroups that form two separate P1A−P2B and P1B−P2A heterodimers on the stalk. So far, structural studies on the P-proteins have not yielded any satisfactory information using either X-ray crystallography or NMR spectroscopy, and the structures of the ribosomal stalk and its individual constituents remain obscure. Here we outline a first, coarse-grained view of the P1A−P2B solution structure obtained by a combination of small-angle X-ray scattering and heteronuclear NMR spectroscopy. The complex has an elongated shape with a length of 10 nm and a cross section of ∼2.5 nm. ^{15}N NMR relaxation measurements establish that roughly 30% of the residues are present in highly flexible segments, which belong primarily to the linker region and the C-terminal part of the polypeptide chain. Secondary structure predictions and NMR chemical shift analysis, together with previous results from CD spectroscopy, indicate that the structured regions involve α-helices. NMR relaxation data further suggest that several helices are arranged in a nearly parallel or antiparallel topology. These results provide the first structural comparison between eukaryotic P1 and P2 proteins and the prokaryotic L12 counterpart, revealing considerable differences in their overall shapes, despite similar functional roles and similar oligomeric arrangements. These results present for the first time a view of the structure of the eukaryotic stalk constituents, which is the only domain of the eukaryotic ribosome that has escaped successful structural characterization.

The three-dimensional (3D) structures of the ribosome, recently determined by X-ray crystallography and cryo-electron microscopy (cryo-EM),[1] have yielded a wealth of information about the mechanism of protein synthesis (*1*). These structural studies have pinpointed several distinct features of functional importance on the ribosome, including the ribosomal stalk, which is composed of several unique proteins (*2*−*5*). This protein complex is functionally conserved in all kingdoms of life and has a central role in the ribosome-mediated stimulation of translation factor-dependent GTP hydrolysis (*6*−*9*). An integrated structural model, based on the prokaryotic stalk structure, has been presented (*10, 11*), but a clear understanding of the structure−function relationships is still lacking for the eukaryotic stalk. Preliminary information about the eukaryotic stalk structure is only available from cryo-EM analyses, which provide a fragmentary view of its shape (*12*−*17*). The ribosomal stalks of prokaryotes and eukaryotes clearly exhibit functional similarity, even though they do not exhibit extensive sequence homology. In eukaryotes, the stalk is composed of three types of P-proteins. The P0 protein is equivalent to

† This work was supported by The Ministry of Science and Higher Education Grant 2 P04A 004 29 to N.G., (2005/2008), European Commission Grant QLK2-CT-2002-00892, and grants from the Swedish Foundation for Strategic Research (SSF) and the Swedish Research Council (VR) awarded to M.A. The SAXS experiments were supported by the European Community-Research Infrastructure Action under the FP6 "Structuring the European Research Area Programme" (Contract RII3/CT/2004/5060008).

* To whom correspondence should be addressed. M.T.: Department of Molecular Biology, Institute of Microbiology and Biotechnology, Maria Curie-Sklodowska University, Akademicka 19, 20-033 Lublin, Poland; telephone, +48-81-5375950; fax, +48-81-5375907; e-mail, maro@hektor.umcs.lublin.pl. M.A.: Department of Biophysical Chemistry, Lund University, P.O. Box 124, SE-221 00 Lund, Sweden; telephone, +46-46-222 8247; fax, +46-46-222 4543; e-mail, mikael.akke@bpc.lu.se.

‡ Maria Curie-Skłdowska University.

§ These two authors contributed equally to this work.

|| Department of Biophysical Chemistry, Lund University.

⊥ European Molecular Biology Laboratory and Russian Academy of Sciences.

@ Department of Molecular Biophysics, Lund University.

Institut de Recerca Biomèdica.

[1] Abbreviations: cryo-EM, cryo-electron microscopy; rRNA, ribosomal RNA; SAXS, small-angle X-ray scattering; NMR, nuclear magnetic resonance; PCR, polymerase chain reaction; SEC, size-exclusion chromatography; DR, dummy residue; NSD, normalized spatial discrepancy; PMSF, phenylmethanesulfonyl fluoride; CTD and NTD, C-terminal and N-terminal domains, respectively.

10.1021/bi0616450 CCC: $37.00
Published on Web 01/30/2007

the L10 protein in prokaryotes and constitutes the stalk base. P0 directly interacts with the conserved sequence of 28S rRNA, and its rRNA binding domain is functionally interchangeable with the corresponding domain in L10 (*18*, *19*). P0 also constitutes the binding site for the two protein dimers, $(P1-P2)_2$ (*20*−*22*), which are composed of two independent polypeptides, P1 and P2 (*23*); this is in contrast to the case in prokaryotes, which contain two to three homodimers of protein L12 (*2*, *10*, *24*). However, in lower eukaryotes such as yeast, two additional subgroups are distinguished, comprising the P1A, P1B, P2A, and P2B proteins (*25*), while an additional P3 protein has been recognized in plants (*26*). The P1 and P2 proteins form biologically relevant P1−P2 heterodimers (*27*−*29*), whereas in yeast, there are two specific P1A−P2B and P1B−P2A heterodimers (*30*−*32*) with differentiated function (*33*). On the basis of the primary structure, the P1 and P2 proteins can be divided into two regions: the N-terminal part of approximately 70 amino acid residues, which mediates the interaction between the P1 and P2 proteins (*34*), and the C-terminal part of around 40 amino acids, in which two segments can be distinguished. The first segment resembles the flexible hinge in the prokaryotic L12 protein, consisting almost exclusively of glycine and alanine, while the second contains a highly conserved stretch of amino acids (EEEAKEESDDDMGFGLFD), including one serine residue which can be phosphorylated in all eukaryotes (*35*, *36*). The last 13 residues of the latter segment have been shown to adopt a turnlike conformation at low temperatures (*37*).

The 3D structure of the P1−P2 protein complex is unknown, and the only structural data come from biophysical characterization of the yeast *Saccharomyces cerevisiae* P1 and P2 proteins. If separated from one another, P1A and P2B become conformationally heterogeneous and show characteristics of "molten globule"-like structures (*38*, *39*). However, they adopt a native structure upon forming the P1A−P2B heterodimer, even in the absence of other ribosomal components (*40*). The P1A−P2B complex is regarded as a key element in the formation of the pentameric stalk structure from both structural and functional points of view (*33*). Existing structural data on the eukaryotic stalk have not provided any satisfactory information about the spatial organization of the stalk constituents, underscoring the fact that this protein complex is very challenging, with respect to both its preparation and behavior in solution.

In this paper, we report the results of small-angle X-ray scattering (SAXS) experiments that determine the overall shape of the isolated yeast P1A−P2B complex. NMR relaxation experiments further aid in characterizing the structural features of the dimer, even though residue-specific resonance assignments were not obtained because of limited sample stability. Together, these data provide a low-resolution structural model for the P1A−P2B complex, which can be described as an elongated molecule with dimensions of 10 nm × 2.5 nm. Our results present the very first view of the eukaryotic ribosomal stalk constituents.

MATERIALS AND METHODS

Sample Preparation. The full-length P1A−P2B protein complex (consisting of 106 residues in P1A and 110 in P2B) was prepared as described previously (*30*, *40*, *41*). The truncated form of the P1A−P2B complex (consisting of 70 residues in P1A and 69 in P2B) was prepared as follows. DNA was amplified with the aid of the polymerase chain reaction (PCR) using specific primers: $\Delta P1A_{1-70}$, 5′-GAG CCA TGG CTA CTG AAT CCG CTT TGT CTT ACG CC-3′ and 5′-GAG CTC GAG ACC AGC TGG GGC AGC AGC ACC-3′; $\Delta P2B_{1-69}$, 5′-GAG CCA TGG CTA AAT ACT TAG CTG CTT ACT TAT TAT TG-3′ and 5′-GAG CTC GAG ACC AGT TGG AAC AGT AGC GAA CTT-3′. PCR fragments were introduced into expression vector pET28 such that a His_6 tag was placed at the C-terminal part of the truncated proteins. All proteins were purified on a Ni-CAM column (Sigma-Aldrich) under denaturing conditions according to the protocol provided by the supplier. The truncated complex was assembled following the denaturing−renaturing procedure used for the full-length P1A−P2B complex (*30*, *40*). Protein concentrations were determined from the absorbance at 280 nm, using an extinction coefficient calculated from the amino acid composition of the full-length yeast P1A−P2B heterocomplex and the truncated form ΔP1A−ΔP2B, following published methods (*42*).

Size-Exclusion Chromatography (SEC). SEC analyses were performed using an Äkta Purifier FPLC system (Amersham Pharmacia Biotech), equipped with a Superose 12 HR 10/30 FPLC analytical gel filtration column. The column was equilibrated with 50 mM Tris-HCl (pH 7.8) and 150 mM NaCl and calibrated using a low-molecular weight protein standard (Amersham Pharmacia Biotech). The flow rate was 0.25 mL/min. The protein elution profile was monitored at 280 nm and analyzed using the UNICORN version 4.0 program supplied with the FPLC system. The molecular mass was estimated as described previously (*30*).

Scattering Experiments and Data Processing. The synchrotron radiation X-ray scattering data were collected in two sessions on the X33 camera (*43*, *44*) at the European Molecular Biology Laboratory (EMBL) on storage ring DORIS III of the Deutsches Elektronen Synchrotron (DESY), using multiwire proportional chambers with delay line readout (*45*). The small-angle scattering patterns from the full-length and truncated version of the heterocomplexes were recorded at several solute concentrations, ranging from 2 to 15 mg/mL. The sample−detector distance was 2.3 m, covering the range of momentum transfer (s) from 0.15 to 3.5 nm^{-1} [$s = 4\pi \sin(\theta)/\lambda$, where 2θ is the scattering angle and λ is the X-ray wavelength (0.15 nm)]. Additionally, the wide-angle scattering from the full-length dimer at a concentration of 22 mg/mL was measured using a sample−detector distance of 1.2 m, covering the s range from 2.4 to 9.8 nm^{-1}. The data were collected in 20 successive 1 min frames and analyzed to verify the absence of radiation damage. Following normalization to the intensity of the transmitted beam, the data were averaged and corrected for the detector response. Scattering due to the buffer was subtracted using PRIMUS (*46*). The difference curves were scaled for protein concentrations and extrapolated to infinite dilution following standard procedures (*47*). For the full-length protein, the data from two measured angular ranges were merged to yield the composite scattering pattern.

The maximum dimensions D_{max} of the full-length dimer and its truncated form were estimated using the orthogonal expansion program ORTOGNOM (*48*). The forward scattering [$I(0)$] and the radius of gyration (R_g) were evaluated

using the Guinier approximation (*49*), assuming that at very small angles ($s < 1.3/R_g$) the intensity is represented as $I(s) = I(0) \exp[-(sR_g)^2/3]$. These parameters were also computed from the entire scattering pattern using the indirect transform package GNOM (*50*), which also provides the distance distribution function $p(r)$ of the particles. The molecular masses of the solutes were evaluated by comparison of the forward scattering with that from a reference solution of bovine serum albumin ($M_r = 66$ kDa).

Ab Initio Scattering Data Analysis. Low-resolution models of the full-length and truncated heterodimers were generated ab initio with GASBOR (*51*). The program represents the protein by an assembly of dummy residues (DRs) and uses simulated annealing to build inside a sphere with the diameter D_{max} a locally "chain-compatible" DR model that fits the experimental data $I_{exp}(s)$ to minimize the residual:

$$\chi^2 = \frac{1}{N-1}\sum_j \left[\frac{I_{exp}(s_j) - cI_{calc}(s_j)}{\sigma(s_j)}\right]^2 \quad (1)$$

where N is the number of experimental points, c is a scaling factor, and $I_{calc}(s_j)$ and $\sigma(s_j)$ are the calculated intensity and the experimental error at the momentum transfer s_j, respectively.

For each solute, results from at least 10 separate GASBOR runs were averaged to determine common structural features using DAMAVER (*52*) and SUPCOMB (*53*). The former generates the average model of the set of automatically superimposed structures and also specifies the most typical model (i.e., the model exhibiting the best agreement with all other models of the set). The program suite DAMAVER (*52*) estimates the stability of the solution provided by ab initio modeling programs. DAMAVER is based on the program SUPCOMB, which aligns two arbitrary low- or high-resolution models by minimizing a normalized spatial discrepancy, NSD (*53*). All pairs of GASBOR models are compared, and the model with the lowest mean value of NSD (the most probable model) is selected as a reference. The remaining models are superimposed with the reference, and the entire assembly is remapped onto a densely packed grid. For each knot of the grid, an occupancy factor is assigned equal to a total overlap volume of a sphere with the diameter equal to the grid edge centered at this grid point with the beads of the entire assembly that are in the vicinity of this point. The averaged model corresponding to an interconnected ensemble of the most populated points is evaluated by filtering the map to yield the volume equal to the average excluded volume of all reconstructions.

Analysis of Secondary Structure Propensity. The amino acid sequences of P1A and P2B were analyzed using multiple secondary structure prediction tools: nnpredict (*54*), PSIPRED (*55*), Sspro (*56*), PredictProtein (*57*), and Jnet (*58*).

NMR Sample Preparation. NMR samples containing either uniformly ^{15}N-labeled P1A in complex with unlabeled P2B, or ^{15}N-labeled P2B in complex with unlabeled P1A, were prepared in 30 mM potassium phosphate buffer (pH 7.5) with 150 mM NaCl, 0.5 mM phenylmethanesulfonyl fluoride (PMSF), and 10% D_2O. The concentration of labeled protein was approximately 0.8 mM, and the sample volume was 650 μL. Samples of the corresponding combinations of $\Delta P1A_{1-70}$ and $\Delta P2B_{1-69}$ were also prepared.

NMR Spectroscopy and Data Processing. NMR data were collected on a Varian Unity Inova 600 MHz spectrometer. ^{15}N R_1 and R_2 relaxation rates and heteronuclear NOEs were measured at 30 ± 0.1 °C following published protocols (*59*). The R_2 experiment employed a CPMG refocusing sequence (*60*, *61*) with a repetition rate of 2222 Hz. R_1 and R_2 relaxation data were acquired with relaxation delays of 0, 60, 140, 200, 280, 420, 560, 840, and 1400 ms and 0, 20, 40, 60, 80, 100, 160, 200, 260, and 300 ms, respectively. All spectra were processed using NMRPipe (*62*). The time domain data were apodized using a cosine window function and zero filled in both dimensions prior to Fourier transformation. Spectra were analyzed using Sparky (*63*). Relaxation rates were obtained by fitting a monoexponential function to the intensity versus time profile for each cross-peak. The heteronuclear ^{1}H−^{15}N NOE was calculated as the ratio of the peak heights in the experiments performed with and without proton saturation.

Analysis of Rotational Diffusion. The rotational diffusion properties for the P1A−P2B complex were determined from the ratio (*64*)

$$\rho = \frac{2R_2'}{R_1'} - 1 = \frac{3}{4}\frac{J(\omega_N)}{J(0)} \quad (2)$$

where R_1' and R_2' are the R_1 and R_2 relaxation rates with the high-frequency spectral density contributions subtracted, respectively, as follows:

$$R_1' = R_1\left[1 - 1.249\left|\frac{\gamma_N}{\gamma_H}\right|(1 - \mathrm{NOE})\right] \quad (3)$$

$$R_2' = R_2 - 1.079\left|\frac{\gamma_N}{\gamma_H}\right|R_1(1 - \mathrm{NOE}) \quad (4)$$

in which γ_N and γ_H are the gyromagnetic ratios for ^{15}N and ^{1}H, respectively. Assuming that chemical exchange is negligible and that the molecule is a spherical particle, ρ depends only on the overall rotational correlation time, τ_c, and the Larmor frequency of ^{15}N, ω_N (*64*)

$$\rho = \frac{3/4}{1 + (\omega_N\tau_c)^2} \quad (5)$$

In the case of a symmetric top, ρ is given by (*64*)

$$\rho = \frac{3/4}{1 + (\omega_N\tau_x)^2}\left\{1 + \frac{(\omega_N\tau_x)^2}{(\omega_N\tau_x)^2 + \left(1 + \frac{1}{6}\epsilon\right)^2} \times \frac{\epsilon \sin^2\theta}{3 + 2\epsilon + \left[1 + \frac{1}{3}\epsilon(2 - 3\sin^2\theta)\right]^2} \times \left\{4 + 3\epsilon + \frac{2}{9}\epsilon^2 - \epsilon\sin^2\theta\left[1 + \frac{4 + \frac{11}{3}\epsilon + \frac{19}{18}\epsilon^2 + \frac{5}{54}\epsilon^3}{(\omega_N\tau_x)^2 + \left(1 + \frac{2}{3}\epsilon\right)^2}\right]\right\}\right\} \quad (6)$$

where $\epsilon = (D_{||}/D_\perp) - 1$, $D_{||}$ is the unique principal value of the diffusion tensor, $D_\perp$ is the value corresponding to the axes orthogonal to the unique principal axis, θ is the angle

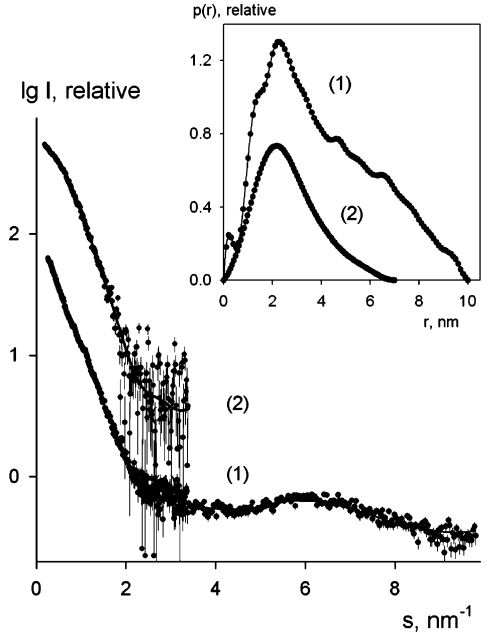

FIGURE 1: Experimental X-ray scattering patterns of the full-length and truncated form of P1A−P2B heterodimers and scattering computed from the models. Dots with error bars depict experimental data, and solid lines are fits obtained from the ab initio models. The inset shows the distance distribution function computed from experimental data by GNOM. Curves 1 and 2 correspond to full-length P1A−P2B and the truncated construct ΔP1A−ΔP2B, respectively.

between the NH bond vector and the unique principal axis, and $\tau_x = (6D_\perp)^{-1}$.

Hydrodynamics Calculations. The rotational diffusion properties of the P1A−P2B complex were predicted from the average SAXS model (Figure 2a), and from the most typical SAXS model (Figure 2b), using HYDRO (*65*). The average and most typical SAXS models consist of beads with radii of 2.5 and 1.9 Å, respectively. The temperature used in the NMR relaxation experiments, 30 °C, and the water viscosity at this temperature, 0.7975 cP, were imposed in the calculations. The hydrodynamic parameters τ_c and $D_{||}/D_\perp$, describing an axially symmetric rotational diffusion tensor, were extracted from the calculations.

RESULTS

Sample Preparation. Following refolding and reconstitution of the intact heterodimer, the overall yield was typically 1 mg of pure P1A−P2B heterodimer per liter of growth medium. The formation of correctly folded heterodimers was verified as described previously (*30*, *40*, *41*). The low yield currently prohibits expensive labeling with stable isotopes for more sophisticated NMR experiments, using, e.g., amino acid-specific labeling schemes. In addition, the samples suffer from limited stability over extended periods of time at room temperature, further preventing residue-specific resonance assignments required for full structure determination of the P1A−P2B complex.

Size Exclusion Chromatography Analysis of the Full-Length and Truncated Heterodimers. We prepared two protein constructs: the full-length P1A−P2B heterodimer and a truncated form ΔP1A−ΔP2B, in which 40 amino acids had been deleted at the C-terminus of both the P1A and P2B proteins. Complex formation and sample homogeneity were

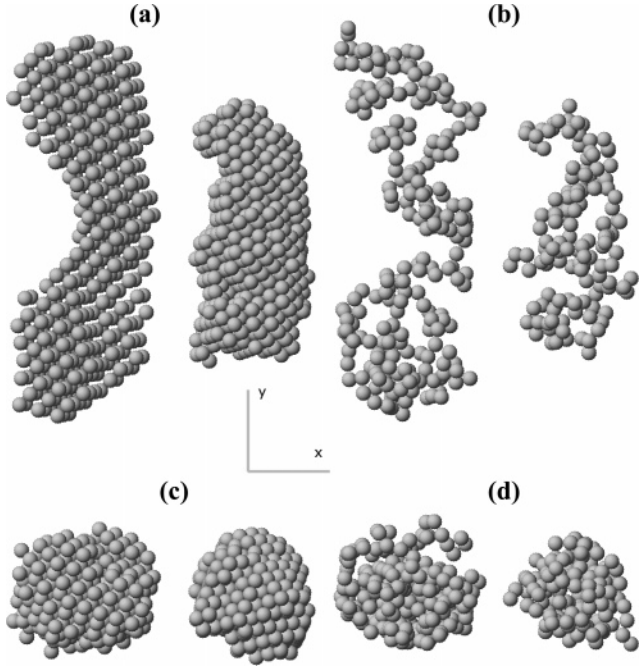

FIGURE 2: Ab initio models of the P1A−P2B heterodimers. In each panel, the full-length P1A−P2B is shown at the left and ΔP1A−ΔP2B at the right: (a and c) averaged shapes and (b and d) most typical dummy residue models. The views in panels c and d show the models in a and b rotated clockwise by 90° around the X-axis, respectively. The models were generated by MASSHA (*82*).

verified by SEC analysis. The elution profile of the P1A−P2B dimer exhibited a symmetrical peak, corresponding to an estimated molecular mass of around 70 kDa, as previously reported (*40*). This value deviates significantly from the theoretical value of 22 kDa predicted from the primary sequence alone. Since the molecular mass estimated by SEC depends on the shape of the analyzed molecule, molecules with highly anisotropic shapes elute with apparent molecular weights that are larger than those of spherical particles. Thus, the result indicates that the heterodimer has an anisotropic shape. SEC analysis of the ΔP1A−ΔP2B complex showed a single symmetrical peak corresponding to a molecular mass of 38 kDa, again departing from the theoretical value (14 kDa), indicating also that the NTD has an anisotropic shape. Comparison of the SEC data for the full-length and truncated complexes suggests that the latter is more compact than the former.

Overall SAXS Parameters. The scattering patterns of the full-length yeast P1A−P2B heterodimer and the truncated form ΔP1A−ΔP2B are presented in Figure 1. The estimated molecular mass of the full-length protein (23 ± 2 kDa) agrees well with the value predicted from the primary sequence (22 kDa), and the same is observed for the truncated heterodimer (experimental value of 14 ± 2 kDa, predicted value of 14 kDa), demonstrating that both dimers yield monodisperse solutions. The distance distribution function $p(r)$ of the full-length P1A−P2B complex (Figure 1, inset, curve 1) suggests an elongated shape with a maximum diameter of ∼10 nm and a cross section of ∼2.5 nm [the latter parameter corresponds to a maximal $p(r)$]. The corresponding data for ΔP1A−ΔP2B (Figure 1, inset, curve 2) yield the same cross section but a maximum dimension of ∼7 nm, showing that this construct has a significantly more compact shape than the full-length complex. The experimental radius of gyration

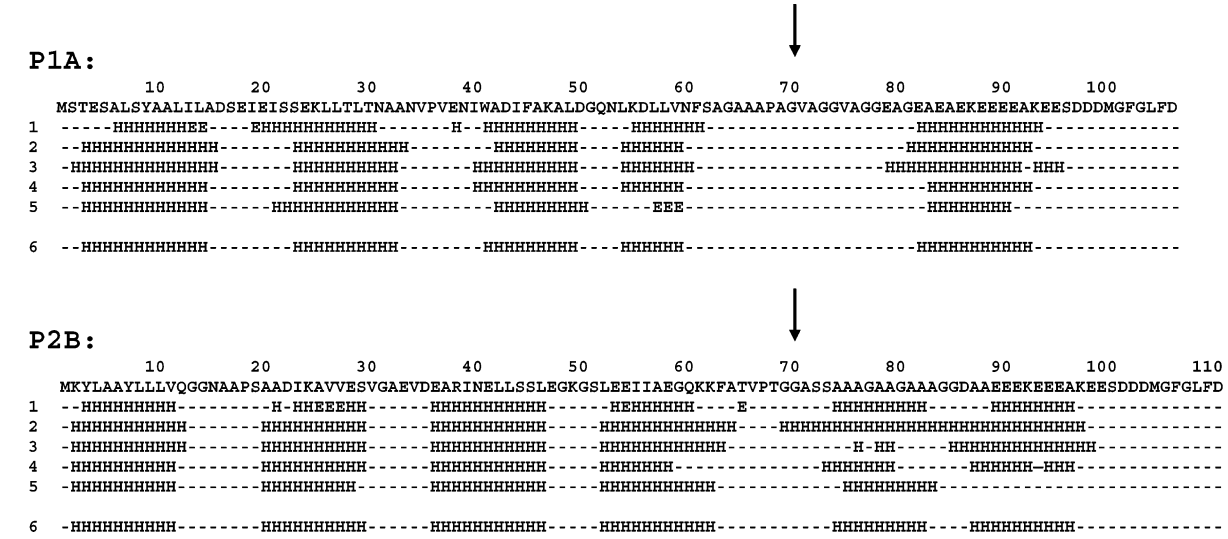

FIGURE 3: Secondary structure predictions of P1A and P2B. The following secondary structure prediction tools were used: (1) Nnpredict, (2) PSIPRED, (3) Sspro, (4) PredictProtein, (5) Jnet, (6) summary assignment, with secondary structure indicated if predicted by at least three of the prediction algorithms. Arrows indicate the ends of truncated forms $\Delta P1A_{1-70}$ and $\Delta P2B_{1-69}$.

of ΔP1A−ΔP2B is also significantly smaller than that of the full-length complex: 2.1 ± 0.1 and 3.2 ± 0.1 nm, respectively.

Shape Determination. To obtain more detailed information about the structure of the P1A−P2B complex, low-resolution models of the full-length and truncated forms of the dimer were reconstructed ab initio from the corresponding experimental scattering patterns, as described in Materials and Methods. Reconstructions using GASBOR yielded superimposable results with consistently good fits to the experimental data, as exemplified by the most typical DR models of the P1A−P2B and ΔP1A−ΔP2B heterodimers with χ values of 1.35 and 0.83, respectively (Figure 1, curves 1 and 2). The averaged models that represent the overall 3D structure of the analyzed dimers are depicted in Figure 2 (a and c). The most typical ab initio models, which represent an ensemble of dummy residues forming chain-compatible models of P1A−P2B and ΔP1A−ΔP2B, are presented in Figure 2 (b and d). The ab initio model of P1A−P2B reveals that the complex is elongated and slightly dumbbell-shaped. In contrast, the model of ΔP1A−ΔP2B does not display a "waist", which may reflect the fact that it does not include the highly flexible C-terminal part (see below). However, the possibility that the uniform cross section of ΔP1A−ΔP2B is a consequence of the lower resolution obtained for ΔP1A−ΔP2B compared to that for P1A−P2B (1.8 and 0.7 nm, respectively) cannot be ruled out. The difference in resolution is attributed to the fact that wide-angle scattering could not be measured for ΔP1A−ΔP2B, because it was not possible to obtain the complex at sufficiently high protein concentrations (cf. curves 1 and 2 of Figure 1).

Secondary Structure Content. Secondary structure predictions based on the amino acid sequence suggest a high helical content, 45% in P1A and 55% in P2B, while the probability for β-strands is very low, as summarized in Figure 3. This prediction agrees well with a previous report based on CD spectroscopy, which showed that the P1A−P2B complex contains 65% α-helical structure on average (*40*). Five α-helices are identified in P1A, comprising residues 3−14, 23−32, 41−49, 54−59, and 82−92. In P2B, six helices are identified, comprising residues 2−11, 20−29, 36−46, 52−62, 74−82, and 87−96. Thus, each protein is predicted to contain four α-helices in its N-terminal part and one (in P1A) or two (in P2B) helices in the C-terminal part, one of which overlaps partly with the highly conserved sequence motif comprising the last 18 residues. The location of the helices matches well between the two proteins, suggesting a common architecture for P1A and P2B.

NMR Spectral Characteristics. The $^1H-^{15}N$ correlation spectra of P1A and P2B reveal a large variation in cross-peak intensity and line widths (Figure 4a,b); a subset of the cross-peaks has sharp and intense line shapes, but the majority is severely broadened. The quality of the spectra indicates that the systems presented here are not amenable to residue-specific chemical shift assignments using ^{15}N-edited spectroscopy. Furthermore, poor protein production yields and limited sample stability hinder the use of more sophisticated labeling schemes. However, it is nonetheless possible to extract useful information about the structure of the P1A−P2B complex, based on statistical analyses of the distributions of the NMR data, even in the absence of residue-specific assignments. Amide proton chemical shifts show a limited variation, with most shifts falling in the interval from 7.3 to 8.7 ppm in both P1A and P2B. The small ^1H chemical shift dispersion suggests that both proteins contain mainly α-helical and unstructured segments (*66*), in agreement with the secondary structure predictions and the data from CD spectroscopy. Parts c and d of Figure 4 show the $^1H-^{15}N$ correlation spectra of the ΔP1A−ΔP2B complex. Pairwise comparisons of parts a and c of Figure 4 and parts b and d of Figure 4 reveal that the great majority of cross-peaks that are sharp and intense in parts a and b are not present in parts c and d, indicating that the C-terminal segments not present in ΔP1A−ΔP2B are highly flexible in the intact proteins (see further below).

^{15}N Spin Relaxation. Relaxation rates were initially quantified for 72 ^{15}N nuclei (68%) in P1A and 107 ^{15}N nuclei (99%) in P2B; the different percentages reflect the difference in spectral quality (cf. Figure 4). For a subset of cross-peaks, the extracted results were unrealistic (for example, some peaks had NOE values greater than 1.0), indicating that the evaluated cross-peaks suffered from overlap. These data were

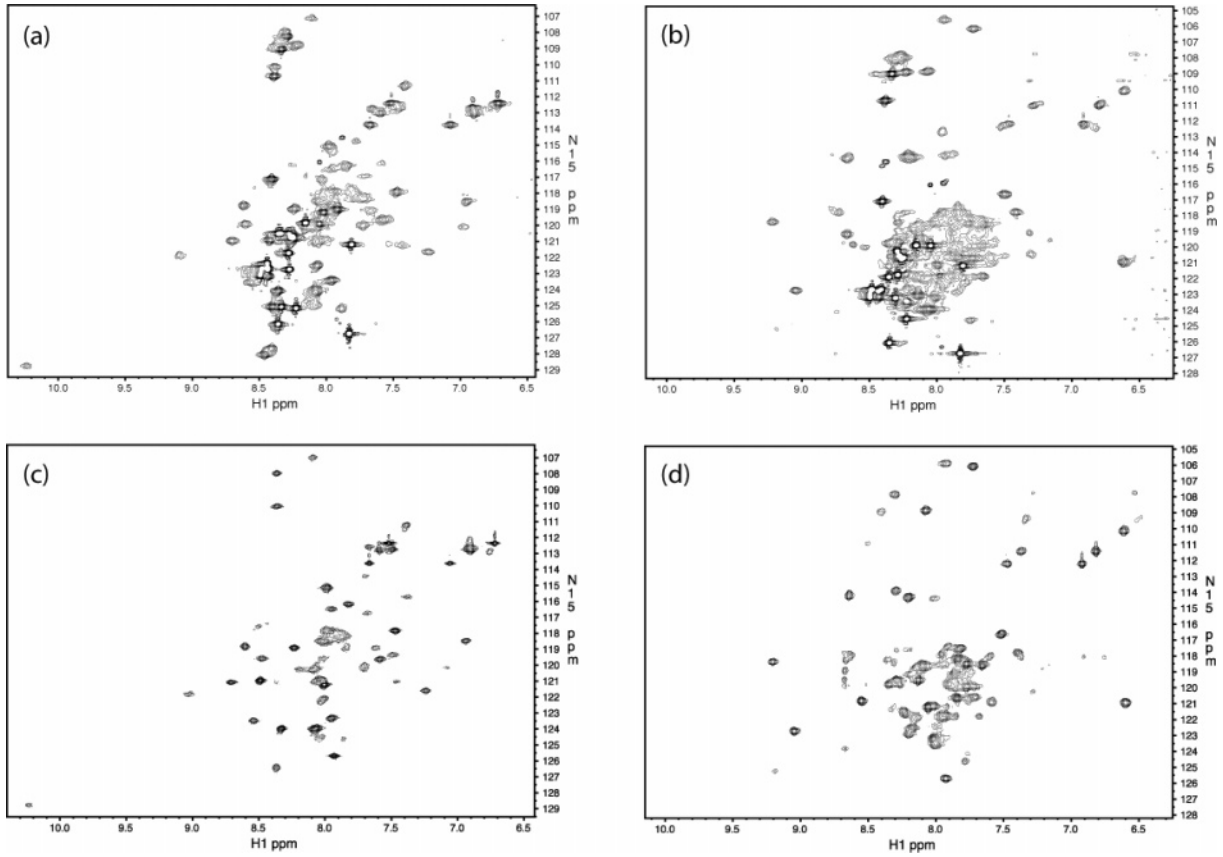

FIGURE 4: $^{1}H-^{15}N$ HSQC NMR spectra of (a) ^{15}N-labeled P1A in complex with unlabeled P2B, (b) ^{15}N-labeled P2B in complex with unlabeled P1A, (c) ^{15}N-labeled ΔP1A in complex with unlabeled ΔP2B, and (d) ^{15}N-labeled ΔP2B in complex with unlabeled ΔP1A.

excluded from further analysis, resulting in a data set comprising 63 (P1A) and 100 (P2B) NH vectors.

R_1 is sensitive to motions on time scales on par with, or shorter than, the effective correlation time for overall rotational diffusion, τ_c. R_2 is dominated by τ_c for NH vectors that experience limited internal dynamics. In addition, R_2 includes contributions from chemical or conformational exchange on the micro- to millisecond time scales. The R_1 values range between 0.34 and 1.83 s^{-1} and between 0.81 and 2.01 s^{-1} for P1A and P2B, respectively. The large variation between different residues reveals significant differences in the amplitudes and time scales of the underlying molecular dynamics. Similarly, R_2 varies significantly with values between 2.1 and 44.4 and between 1.7 and 43.8 s^{-1} for P1A and P2B, respectively. There are no cases of specific residues with very large values of R_2, suggesting that conformational exchange is not a major factor in the relaxation of these proteins. However, this set of relaxation experiments cannot identify moderate exchange affecting extensive regions of the proteins (*67*, *68*).

The heteronuclear NOE is a sensitive reporter of intramolecular high-frequency motions. The NOE values show a significant variation between −1.7 and 1.0 in both P1A and P2B (Figure 5). The variations in NOE values indicate that highly flexible segments coexist with well-formed secondary structure elements in both proteins. NOE values greater than 0.5 correspond to intramolecular dynamics of limited amplitude, typical for secondary structure elements (*69*). Given this criterion, the data shown in Figure 5a imply that at least 23 residues (22%) in P1A are located in well-formed secondary structure elements. Correspondingly, Figure 5b suggests that at least 47 residues (43%) in P2B are located in secondary structure elements. These values are lower limits, and the actual ones are most likely higher, because highly flexible residues have sharp cross-peaks, which are easier to identify and quantify accurately than the broadened peaks that belong to structured residues. In the case of the P2B data set, which is more complete, the percentage (43%) agrees reasonably well with that from the secondary structure predictions (55%). In both proteins, many residues are highly flexible. The large proportion of residues with a NOE of <0, viz., 32 (30%) in P1A and 32 (32%) in P2B, suggests that the majority of the flexible residues have random coil-like properties. Detailed comparisons of the spectra in parts a and c of Figure 4 reveal that 21 cross-peaks clearly identified in Figure 4a are not present in Figure 4c. Twenty of these cross-peaks have a NOE of <0, while the remaining one had an anomalous NOE and was excluded from the analysis outlined above. Similarly, 23 cross-peaks presented in Figure 4b are not visible in Figure 4d, and all of these have NOEs of <0. Thus, at least 56% of the residues in the C-terminal segments are highly flexible (20 of 36 residues in P1A and 23 of 41 in P2B). Conversely, there are 12 residues in the N-terminal parts of both P1A and P2B with NOEs of <0.

Rotational Diffusion Properties. Values of ρ were calculated from the R_1 and R_2 rates for the structured residues with NOEs of >0.5, yielding 23 and 47 data points for P1A and P2B, respectively (Figure 5). Figure 6 shows the resulting data plotted in increasing order of ρ. As described by eq 5, the ρ value should be constant for a spherical complex. This is clearly not the case for the P1A−P2B complex, which

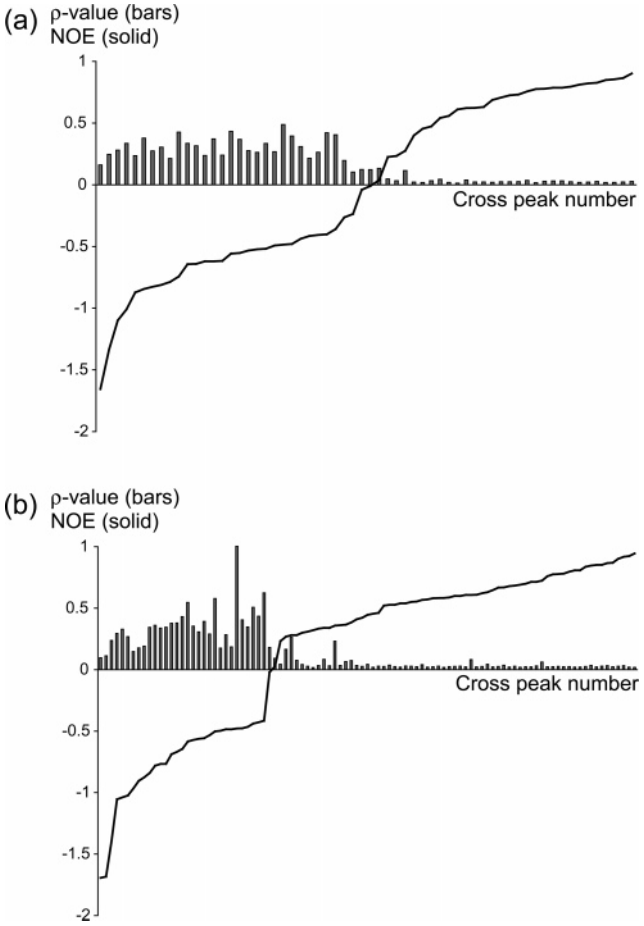

FIGURE 5: Distributions of protein backbone amide ρ values (bars) and heteronuclear $^1H-^{15}N$ NOE values (solid line), sorted according to NOE values: (a) data for residues in P1A in complex with P2B and (b) data for residues in P2B in complex with P1A.

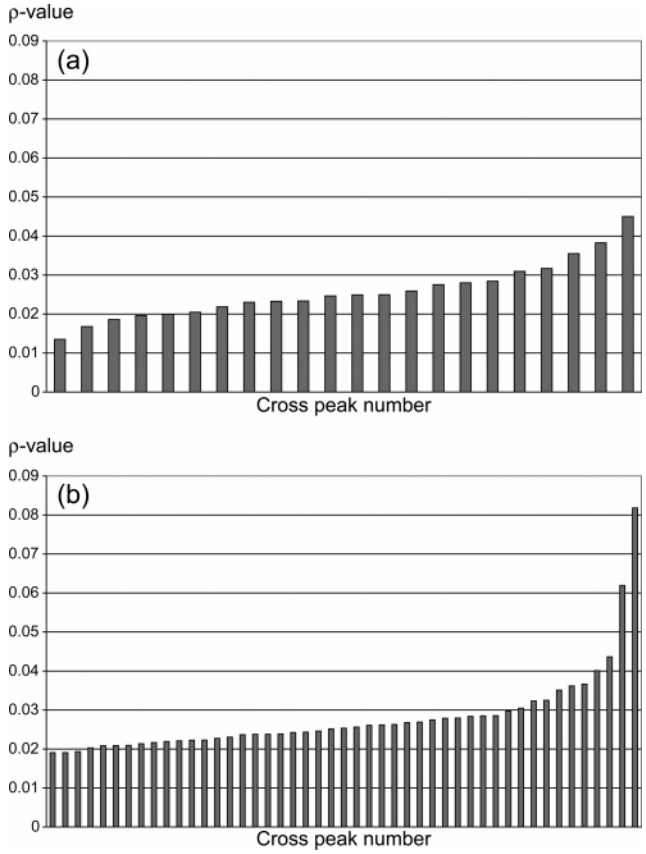

FIGURE 6: Distribution of protein backbone amide ρ values for (a) P1A in complex with P2B and (b) P2B in complex with P1A. Data are shown only for structured residues, i.e., those with heteronuclear $^1H-^{15}N$ NOE values greater than 0.5.

instead has a profile of ρ values corresponding to an anisotropic diffusion tensor, in agreement with the SAXS data presented above. Given that the complex is a symmetric top, a minimum value for the anisotropy can be calculated using eq 6 by assuming that the lowest and highest values of ρ correspond to NH vectors that are oriented parallel ($\theta = 0°$) and perpendicular ($\theta = 90°$), respectively, to the principal axis of the rotational diffusion tensor. The data presented here for the P1A−P2B complex yield a minimum anisotropy ($D_{||}/D_{\perp}$) of 5.6 and a minimum $D_{\perp}$ value of 8.6×10^6 s^{-1}, corresponding to a $\tau_{\perp}$ of 19 ns and a $\tau_{||}$ of 3.5 ns, which results in an effective correlation time τ_c of 7.6 ns. Considering that some 30% of the complex consists of unstructured residues, this value agrees reasonably well with the τ_c of 13 ns expected for a spherical top with the same molecular mass as the P1A−P2B complex (*70*, *71*). Trimming of the data to exclude the highest ρ value yields $D_{||}/D_{\perp}$ of 4.1 and a τ_c of 9.5 ns. Hydrodynamics calculations based on the most typical ab initio SAXS model from GASBOR (Figure 2b) yield an anisotropy $D_{||}/D_{\perp}$ of 3.6 and an effective correlation time (τ_c) of 14.4 ns. For comparison, calculations based on the average SAXS model (Figure 2a) result in a smaller $D_{||}/D_{\perp}$ of 2.5 and a significantly larger τ_c of 23 ns. Discrepancies between hydrodynamic properties predicted from SAXS and ^{15}N relaxation are expected in this case, because ab initio shape determination using SAXS data from partly flexible systems requires an artificially large number of beads to represent the flexible segments. Consequently, the resulting number of beads is unrealistic with respect to the amount of mass that the beads represent. Thus, a larger τ_c and a smaller degree of anisotropy are expected from theoretical calculations performed on ab initio SAXS models, compared with those derived from relaxation experiments. Considering these issues, the results from ^{15}N relaxation and SAXS are in reasonable agreement.

The most common value of ρ for an axially symmetric molecule with a random distribution of NH bond vector orientations corresponds to the plane associated with $D_{\perp}$, i.e., $\theta = 90°$. This is also the orientation that gives the largest value of ρ. Figure 6 shows that the distribution obtained for the P1A−P2B complex reflects the opposite scenario, where small values of ρ are favored, indicating that the most common orientation of the NH bond vectors is close to the unique principal axis associated with $D_{||}$. θ can be estimated for each residue from its value of ρ and the global anisotropy parameters $D_{||}$ and $D_{\perp}$ presented above. Figure 7 shows a histogram of the number of residues with a given value of θ. In the structured parts of P1A and P2B, 16 NH bond vectors (of 22) and 33 (of 47), respectively, have θ angles of $<30°$, with the majority having an angle θ between 20° and 30° (13 in P1A and 30 in P2B). In α-helices, the angle between an NH bond vector and the helix axis is approximately 15°. Thus, our results imply that most residues in the structured regions of P1A and P2B are located in helices that are close to parallel to the unique axis of the overall diffusion tensor. According to the secondary structure

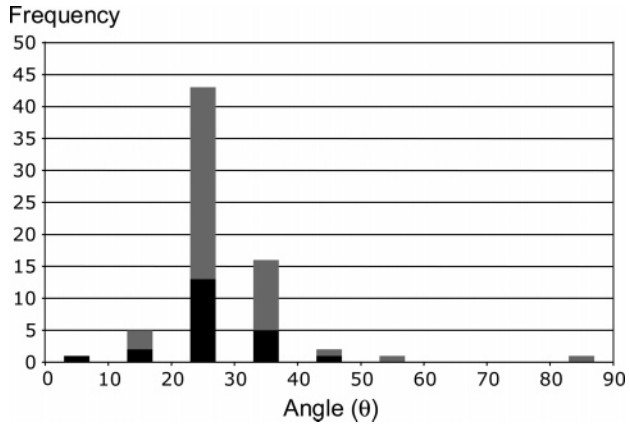

FIGURE 7: Histogram of the calculated θ angles between the $^1H-^{15}N$ amide bond vectors and the unique principal axis of the rotational diffusion tensor. Data for P1A and P2B are shown as black and gray bars, respectively. The angles were calculated using eq 6, assuming that the largest and smallest values of ρ correspond to θ values of 90° and 0°, respectively. Data are included only for those residues that have NOEs of >0.5.

prediction, each of the α-helices in the P1A−P2B complex is approximately 10 residues long. Together with the relaxation data, this suggests that at least two helices in P1A and three helices in P2B are oriented along the long axis of the molecular shape depicted in Figure 2A.

DISCUSSION

In this study, we have outlined the structure of the yeast P1A−P2B heterodimer, using SAXS and NMR, thereby providing the very first structural insight into the eukaryotic ribosomal stalk components. The eukaryotic stalk is the only remaining ribosomal element that has not been structurally characterized at low and high resolution. Despite much effort in the past, crystals suitable for X-ray diffraction have not been obtained. In addition, structural studies are hampered because the preparation of the protein complex is very demanding and results in very low yields, which effectively limits the production of isotope-enriched protein samples for detailed NMR studies. What is more, the resulting samples have limited stability at room temperature, further impeding full structure determination of the yeast complex by NMR spectroscopy.

Results from SAXS and NMR relaxation independently indicate that the complex has an elongated shape. The SAXS analysis shows that the P1A−P2B dimer has a maximum diameter of ∼10 nm and a cross section of ∼2.5 nm, while ΔP1A−ΔP2B has the same cross section as the intact complex but a shorter maximum length of ∼7 nm. The C-terminal segments that are absent in ΔP1A−ΔP2B may be located at both apexes of the model describing the full-length dimer, but a parallel arrangement cannot be excluded (Figure 2). This is in agreement with the NMR relaxation data, which demonstrate that at least 50% of the residues in the C-terminal segments (including part of the hinge regions) of P1A−P2B are highly flexible. On the basis of these observations, we speculate that the movement of the C-terminal segments relative to the central NTD dimer makes them appear to have wider cross sections than the central portions, which is evident from Figure 2.

Comparing the model of P1A−P2B presented here with the 3D structure of bacterial L12, we can notice significant differences. The L12 N-terminal domain (NTD) dimer comprises roughly 35 residues from each polypeptide, which are arranged as two antiparallel α-hairpins, resulting in a symmetrical four-helix bundle with a globular shape and a maximum diameter of ∼2.4 nm (*72*). In contrast, the N-terminal dimer represented by the ΔP1A−ΔP2B construct contains approximately twice the number of residues, hypothetically arranged into eight α-helices, as predicted from the secondary structure propensities and generally supported by the NMR data. The NMR relaxation data reveal that at least 22% of the residues in P1A and 43% in P2B are located in well-formed secondary structure elements, which most likely are α-helices as gauged from NMR chemical shifts and secondary structure predictions. Given that the average length of the predicted α-helices is 10 residues, these results suggest that P1A and P2B contain at least two and four well-structured helices, respectively. Again, we emphasize that these numbers represent lower bounds. The ΔP1A−ΔP2B dimer is more elongated than the NTD dimer of L12, with a significantly larger maximum diameter (7 nm vs 2.4 nm), demonstrating that there is no direct correspondence in the overall shape between the NTD dimers of the P1 and P2 proteins and L12. The size discrepancy between the NTD P1A−P2B dimers and L12 is underscored by the fact that the interface between L10 and the NTD dimer of L12 comprises only 10 amino acids of L10 (*10*), whereas 30 amino acids of P0 are involved in anchoring the NTD dimer of the P1 and P2 proteins to P0 (*22*).

However, the rotational diffusion analysis of the NMR relaxation data suggests that at least five helices in the P1A−P2B complex are oriented with their axes close to parallel to the long axis of the dimer (Figure 7). This result may indicate that helical bundles also occur in the P1A−P2B NTD dimer, just as in L12. The current results are thus compatible with a model for the P1A−P2B NTD dimer that involves a sequential arrangement of two four-helix bundles, although several other models are also conceivable. It seems possible that extensive domain swapping may take place between the NTDs of the two proteins, because dimer formation in vitro is achieved only after a sequential denaturation−renaturation process of P1A and P2B (*30*, *40*). At this stage, it is not possible to conclude whether the arrangement of P1A and P2B in the dimer is parallel or antiparallel.

The NMR data further demonstrate that approximately 30% of the residues in the P1A−P2B complex (20 and 23 in the C-terminal segment of P1A and P2B, respectively, and 12 in each N-terminal segment) are located in largely unstructured segments with NOEs of <0. The former group represents 56% of the total number of residues in the C-terminal segments, demonstrating that this polypeptide fragment contains a highly flexible region. However, the available NMR data are also consistent with the presence of structured elements in the C-terminal segments, as predicted from the secondary structure propensities. Indeed, previous work indicates that the 13 C-terminal amino acids have a preference for a turnlike conformation at low temperatures (*37*). In addition to the highly flexible residues (NOE < 0), there 7 (in P1A) and 20 (in P2B) additional residues with NOEs between 0 and 0.5, which implies that these also are located outside of well-formed secondary structure elements.

The consensus secondary structure propensities (Figure 3) predict that intervening segments of four to eight residues are present between the helices in the NTD, yielding around 20 residues connecting the helices in total for P1A and P2B. Residues located in loops between secondary structure elements are often exposed and exhibit higher degrees of flexibility than those in helices (*73*). Thus, the experimentally determined number of residues outside of well-formed secondary structure elements matches well that expected from the secondary structure predictions in the case of P2B, for which the experimental data are almost complete.

The C-terminal segment constitutes the functional part of both L12 and P1A−P2B. The C-terminal domain (CTD) of L12 (residues 53−120; *E. coli* numbering) adopts a compact globular α/β fold (*72*, *74*, *75*). In contrast, the highly conserved C-terminal region of the P-proteins comprises only some 20 residues (*4*) and does not appear to form a compact domain, although the first half of this region has a propensity to form an α-helix (Figure 3) and the second half folds into a turnlike conformation at low temperatures (*37*). In this context, it is worth noting that the dominant interactions between L12 and translation factors involve a conserved region of an α-helix (*76*, *77*), possibly suggesting that the corresponding feature has been preserved in eukaryotes but occurs in a different structural context.

In prokaryotes, the CTD is connected to the NTD through a disordered hinge region (residues 35−52) (*78*, *79*), which is an indispensable element of the stalk activity (*80*). The hinge region has a high proportion of hydrophobic residues (viz., valine and alanine) with high helix propensities, suggesting that the observed disorder may reflect rapid interconversion between helix and coil conformations (*72*, *75*, *81*). In eukaryotes, a similar stretch of valine, alanine, and glycine residues is present, but it is located closer to the C-terminal end of the polypeptide; in yeast, its location is between residues 65 and 85. The hinge region in eukaryotes is also expected to be flexible, as inferred from the sequence homology to its prokaryotic counterpart and further supported by the NMR data. However, in P2B, but not in P1A, the hinge region may have a high propensity for helix formation (Figure 3).

In summary, these results reveal that the P1 and P2 proteins and the prokaryotic L12, despite similar functional roles and similar oligomeric arrangements, differ considerably in their overall shapes. Nonetheless, the two proteins share certain common structural features; both proteins include a highly flexible hinge segment between the NTD and CTD, and the P1A−P2B NTD apparently consists of helical bundles, just as the NTD of L12. However, the eukaryotic NTD dimer is considerably more elongated and apparently includes twice as many α-helices as the NTD dimer of L12. Furthermore, the C-terminal region of P1A−P2B is very different from the CTD of L12. From the available structural information, it appears that the common biological function was preserved in few structural elements and is based on the following features: the NTD dimer anchors the protein to the ribosome, and the flexible hinge gives the CTD the orientational freedom to contact factor binding sites on the ribosome and to aid in catalyzing GTP hydrolysis by the translational G-proteins.

REFERENCES

1. Liljas, A. (2004) *Structural Aspects of Protein Synthesis*, World Scientific Publishing, Singapore.
2. Wahl, M. C., and Moller, W. (2002) Structure and function of the acidic ribosomal stalk proteins, *Curr. Protein Pept. Sci. 3*, 93−106.
3. Gonzalo, P., and Reboud, J. P. (2003) The puzzling lateral flexible stalk of the ribosome, *Biol. Cell 95*, 179−193.
4. Tchorzewski, M. (2002) The acidic ribosomal P proteins, *Int. J. Biochem. Cell Biol. 34*, 911−915.
5. Ballesta, J. P., and Remacha, M. (1996) The large ribosomal subunit stalk as a regulatory element of the eukaryotic translational machinery, *Prog. Nucleic Acid Res. Mol. Biol. 55*, 157−193.
6. van Agthoven, A. J., Maassen, J. A., and Moller, W. (1977) Structure and phosphorylation of an acidic protein from 60S ribosomes and its involvement in elongation factor-2 dependent GTP hydrolysis, *Biochem. Biophys. Res. Commun. 77*, 989−998.
7. Kischa, K., Moller, W., and Stoffler, G. (1971) Reconstitution of a GTPase activity by a 50S ribosomal protein and *E. coli*, *Nat. New Biol. 233*, 62−63.
8. Savelsbergh, A., Mohr, D., Wilden, B., Wintermeyer, W., and Rodnina, M. V. (2000) Stimulation of the GTPase activity of translation elongation factor G by ribosomal protein L7/12, *J. Biol. Chem. 275*, 890−894.
9. Mohr, D., Wintermeyer, W., and Rodnina, M. V. (2002) GTPase activation of elongation factors Tu and G on the ribosome, *Biochemistry 41*, 12520−12528.
10. Diaconu, M., Kothe, U., Schlunzen, F., Fischer, N., Harms, J. M., Tonevitsky, A. G., Stark, H., Rodnina, M. V., and Wahl, M. C. (2005) Structural Basis for the Function of the Ribosomal L7/12 Stalk in Factor Binding and GTPase Activation, *Cell 121*, 991−1004.
11. Datta, P. P., Sharma, M. R., Qi, L., Frank, J., and Agrawal, R. K. (2005) Interaction of the G′ Domain of Elongation Factor G and the C-Terminal Domain of Ribosomal Protein L7/L12 during Translocation as Revealed by Cryo-EM, *Mol. Cell 20*, 723−731.
12. Beckmann, R., Bubeck, D., Grassucci, R., Penczek, P., Verschoor, A., Blobel, G., and Frank, J. (1997) Alignment of conduits for the nascent polypeptide chain in the ribosome-Sec61 complex, *Science 278*, 2123−2126.
13. Gomez-Lorenzo, M. G., Spahn, C. M., Agrawal, R. K., Grassucci, R. A., Penczek, P., Chakraburtty, K., Ballesta, J. P., Lavandera, J. L., Garcia-Bustos, J. F., and Frank, J. (2000) Three-dimensional cryo-electron microscopy localization of EF2 in the *Saccharomyces cerevisiae* 80S ribosome at 17.5 Å resolution, *EMBO J. 19*, 2710−2718.
14. Spahn, C. M., Gomez-Lorenzo, M. G., Grassucci, R. A., Jorgensen, R., Andersen, G. R., Beckmann, R., Penczek, P. A., Ballesta, J. P., and Frank, J. (2004) Domain movements of elongation factor eEF2 and the eukaryotic 80S ribosome facilitate tRNA translocation, *EMBO J. 23*, 1008−1019.
15. Spahn, C. M., Jan, E., Mulder, A., Grassucci, R. A., Sarnow, P., and Frank, J. (2004) Cryo-EM visualization of a viral internal ribosome entry site bound to human ribosomes: The IRES functions as an RNA-based translation factor, *Cell 118*, 465−475.
16. Spahn, C. M., Beckmann, R., Eswar, N., Penczek, P. A., Sali, A., Blobel, G., and Frank, J. (2001) Structure of the 80S ribosome from *Saccharomyces cerevisiae*: tRNA-ribosome and subunit-subunit interactions, *Cell 107*, 373−386.
17. Morgan, D. G., Menetret, J. F., Radermacher, M., Neuhof, A., Akey, I. V., Rapoport, T. A., and Akey, C. W. (2000) A comparison of the yeast and rabbit 80S ribosome reveals the topology of the nascent chain exit tunnel, inter-subunit bridges and mammalian rRNA expansion segments, *J. Mol. Biol. 301*, 301−321.
18. Uchiumi, T., Hori, K., Nomura, T., and Hachimori, A. (1999) Replacement of L7/L12.L10 protein complex in *Escherichia coli* ribosomes with the eukaryotic counterpart changes the specificity of elongation factor binding, *J. Biol. Chem. 274*, 27578−27582.
19. Santos, C., and Ballesta, J. P. (2005) Characterization of the 26S rRNA-binding domain in *Saccharomyces cerevisiae* ribosomal stalk phosphoprotein P0, *Mol. Microbiol. 58*, 217−226.
20. Santos, C., and Ballesta, J. P. (1995) The highly conserved protein P0 carboxyl end is essential for ribosome activity only in the absence of proteins P1 and P2, *J. Biol. Chem. 270*, 20608−20614.
21. Hagiya, A., Naganuma, T., Maki, Y., Ohta, J., Tohkairin, Y., Shimizu, T., Nomura, T., Hachimori, A., and Uchiumi, T. (2005)

A Mode of Assembly of P0, P1, and P2 Proteins at the GTPase-associated Center in Animal Ribosome: In Vitro Analyses with P0 Truncation Mutants, *J. Biol. Chem. 280*, 39193−39199.
22. Krokowski, D., Boguszewska, A., Abramczyk, D., Liljas, A., Tchorzewski, M., and Grankowski, N. (2006) Yeast ribosomal P0 protein has two separate binding sites for P1/P2 proteins, *Mol. Microbiol. 60*, 386−400.
23. Wool, I. G., Chan, Y. L., Gluck, A., and Suzuki, K. (1991) The primary structure of rat ribosomal proteins P0, P1, and P2 and a proposal for a uniform nomenclature for mammalian and yeast ribosomal proteins, *Biochimie 73*, 861−870.
24. Ilag, L. L., Videler, H., McKay, A. R., Sobott, F., Fucini, P., Nierhaus, K. H., and Robinson, C. V. (2005) Heptameric (L12)6/L10 rather than canonical pentameric complexes are found by tandem MS of intact ribosomes from thermophilic bacteria, *Proc. Natl. Acad. Sci. U.S.A. 102*, 8192−8197.
25. Planta, R. J., and Mager, W. H. (1998) The list of cytoplasmic ribosomal proteins of *Saccharomyces cerevisiae*, *Yeast 14*, 471−477.
26. Szick, K., Springer, M., and Bailey-Serres, J. (1998) Evolutionary analyses of the 12-kDa acidic ribosomal P-proteins reveal a distinct protein of higher plant ribosomes, *Proc. Natl. Acad. Sci. U.S.A. 95*, 2378−2383.
27. Tchorzewski, M., Boldyreff, B., Issinger, O., and Grankowski, N. (2000) Analysis of the protein-protein interactions between the human acidic ribosomal P-proteins: Evaluation by the two hybrid system, *Int. J. Biochem. Cell Biol. 32*, 737−746.
28. Gonzalo, P., Lavergne, J. P., and Reboud, J. P. (2001) Pivotal role of the P1 N-terminal domain in the assembly of the mammalian ribosomal stalk and in the proteosynthetic activity, *J. Biol. Chem. 276*, 19762−19769.
29. Shimizu, T., Nakagaki, M., Nishi, Y., Kobayashi, Y., Hachimori, A., and Uchiumi, T. (2002) Interaction among silkworm ribosomal proteins P1, P2 and P0 required for functional protein binding to the GTPase-associated domain of 28S rRNA, *Nucleic Acids Res. 30*, 2620−2627.
30. Tchorzewski, M., Boguszewska, A., Dukowski, P., and Grankowski, N. (2000) Oligomerization properties of the acidic ribosomal P-proteins from *Saccharomyces cerevisiae*: Effect of P1A protein phosphorylation on the formation of the P1A-P2B hetero-complex, *Biochim. Biophys. Acta 1499*, 63−73.
31. Guarinos, E., Remacha, M., and Ballesta, J. P. (2001) Asymmetric interactions between the acidic P1 and P2 proteins in the *Saccharomyces cerevisiae* ribosomal stalk, *J. Biol. Chem. 276*, 32474−32479.
32. Abramczyk, D., Tchorzewski, M., Krokowski, D., Boguszewska, A., and Grankowski, N. (2004) Overexpression, purification and characterization of the acidic ribosomal P-proteins from *Candida albicans*, *Biochim. Biophys. Acta 1672*, 214−223.
33. Krokowski, D., Tchorzewski, M., Boguszewska, A., and Grankowski, N. (2005) Acquisition of a stable structure by yeast ribosomal P0 protein requires binding of P1A-P2B complex: In vitro formation of the stalk structure, *Biochim. Biophys. Acta 1724*, 59−70.
34. Jose, M. P., Santana-Roman, H., Remacha, M., Ballesta, J. P., and Zinker, S. (1995) Eukaryotic acidic phosphoproteins interact with the ribosome through their amino-terminal domain, *Biochemistry 34*, 7941−7948.
35. Hasler, P., Brot, N., Weissbach, H., Parnassa, A. P., and Elkon, K. B. (1991) Ribosomal proteins P0, P1, and P2 are phosphorylated by casein kinase II at their conserved carboxyl termini, *J. Biol. Chem. 266*, 13815−13820.
36. Ballesta, J. P., Rodriguez-Gabriel, M. A., Bou, G., Briones, E., Zambrano, R., and Remacha, M. (1999) Phosphorylation of the yeast ribosomal stalk. Functional effects and enzymes involved in the process, *FEMS Microbiol. Rev. 23*, 537−550.
37. Soares, M. R., Bisch, P. M., Campos de Carvalho, A. C., Valente, A. P., and Almeida, F. C. (2004) Correlation between conformation and antibody binding: NMR structure of cross-reactive peptides from *T. cruzi*, human and *L. braziliensis*, *FEBS Lett. 560*, 134−140.
38. Zurdo, J., Sanz, J. M., Gonzalez, C., Rico, M., and Ballesta, J. P. (1997) The exchangeable yeast ribosomal acidic protein YP2β shows characteristics of a partly folded state under physiological conditions, *Biochemistry 36*, 9625−9635.
39. Zurdo, J., Gonzalez, C., Sanz, J. M., Rico, M., Remacha, M., and Ballesta, J. P. (2000) Structural differences between *Saccharomyces cerevisiae* ribosomal stalk proteins P1 and P2 support their functional diversity, *Biochemistry 39*, 8935−8943.
40. Tchorzewski, M., Krokowski, D., Boguszewska, A., Liljas, A., and Grankowski, N. (2003) Structural characterization of yeast acidic ribosomal P proteins forming the P1A-P2B heterocomplex, *Biochemistry 42*, 3399−3408.
41. Tchorzewski, M., Boguszewska, A., Abramczyk, D., and Grankowski, N. (1999) Overexpression in *Escherichia coli*, purification, and characterization of recombinant 60S ribosomal acidic proteins from *Saccharomyces cerevisiae*, *Protein Expression Purif. 15*, 40−47.
42. Gill, S. C., and von Hippel, P. H. (1989) Calculation of protein extinction coefficients from amino acid sequence data, *Anal. Biochem. 182*, 319−326.
43. Boulin, C. J., Kempf, R., Gabriel, A., and Koch, M. H. J. (1988) Data acquisition systems for linear and area X-ray detectors using delay line readout, *Nucl. Instrum. Methods 269*, 312−320.
44. Koch, M. H. J., and Bordas, J. (1983) X-ray diffraction and scattering on disordered systems using synchrotron radiation, *Nucl. Instrum. Methods 208*, 461−469.
45. Gabriel, A., and Dauvergne, F. (1982) The localization method used at EMBL, *Nucl. Instrum. Methods 201*, 223−224.
46. Konarev, P. V., Volkov, V. V., Sokolova, A. V., Koch, M. H. J., and Svergun, D. I. (2003) PRIMUS: A Windows-PC based system for small-angle scattering data analysis, *J. Appl. Crystallogr. 36*, 1277−1282.
47. Feigin, L. A., and Svergun, D. I. (1987) *Structure analysis by small-angle X-ray and neutron scattering*, Plenum Press, New York.
48. Svergun, D. I. (1993) A direct indirect method of small-angle scattering data treatment, *J. Appl. Crystallogr. 26*, 258−267.
49. Guinier, A. (1939) La diffraction des rayons X aux tres petits angles; application a l'etude de phenomenes ultramicroscopiques, *Ann. Phys. (Paris, Fr.) 12*, 161−237.
50. Svergun, D. I. (1992) Determination of the regularization parameter in indirect transform methods using perceptual criteria, *J. Appl. Crystallogr. 25*, 495−503.
51. Svergun, D. I., Petoukhov, M. V., and Koch, M. H. (2001) Determination of domain structure of proteins from X-ray solution scattering, *Biophys. J. 80*, 2946−2953.
52. Volkov, V. V., and Svergun, D. I. (2003) Uniqueness of ab initio shape determination in small angle scattering, *J. Appl. Crystallogr. 36*, 860−864.
53. Kozin, M. B., and Svergun, D. I. (2001) Automated matching of high- and low-resolution structural models, *J. Appl. Crystallogr. 34*, 33−41.
54. Kneller, D. G., Cohen, F. E., and Langridge, R. (1990) Improvements in protein secondary structure prediction by an enhanced neural network, *J. Mol. Biol. 214*, 171−182.
55. McGuffin, L. J., Bryson, K., and Jones, D. T. (2000) The PSIPRED protein structure prediction server, *Bioinformatics 16*, 404−405.
56. Pollastri, G., Przybylski, D., Rost, B., and Baldi, P. (2002) Improving the prediction of protein secondary structure in three and eight classes using recurrent neural networks and profiles, *Proteins 47*, 228−235.
57. Rost, B., Sander, C., and Schneider, R. (1994) PHD: An automatic mail server for protein secondary structure prediction, *Comput. Appl. Biosci. 10*, 53−60.
58. Cuff, J. A., Clamp, M. E., Siddiqui, A. S., Finlay, M., and Barton, G. J. (1998) JPred: A consensus secondary structure prediction server, *Bioinformatics 14*, 892−893.
59. Farrow, N. A., Muhandiram, R., Singer, A. U., Pascal, S. M., Kay, C. M., Gish, G., Shoelson, S. E., Pawson, T., Forman-Kay, J. D., and Kay, L. E. (1994) Backbone Dynamics of a Free and Phosphopeptide-Complexed Src Homology 2 Domain Studied by ^{15}N NMR Relaxation, *Biochemistry 33*, 5984−6003.
60. Carr, H. Y., and Purcell, E. M. (1954) Effects of Diffusion on Free Precession in Nuclear Magnetic Resonance Experiments, *Phys. Rev. 94*, 630−638.
61. Meiboom, S., and Gill, D. (1958) Modified Spin-Echo Method for Measuring Nuclear Relaxation Times, *Rev. Sci. Instrum. 29*, 688−691.
62. Delaglio, F., Grzesiek, S., Vuister, G., Zhu, G., Pfeifer, J., and Bax, A. (1995) NMRPipe: A multidimensional spectral processing system based on UNIX Pipes, *J. Biomol. NMR 6*, 277−293.
63. Goddard, T. D., and Kneller, D. G. (2004) *Sparky*, University of California, San Francisco.
64. Fushman, D., Varadan, R., Assfalg, M., and Walker, O. (2004) Determining domain orientation in macromolecules by using spin-relaxation and residual dipolar coupling measurements, *Prog. Nucl. Magn. Reson. Spectrosc. 44*, 189−214.

65. Garcia de la Torre, J., Navarro, S., Lopez Martinez, M. C., Diaz, F. G., and Lopez Cascales, J. J. (1994) HYDRO: A computer program for the prediction of hydrodynamic properties of macromolecules, *Biophys. J. 67*, 530−531.
66. Wishart, D. S., and Sykes, B. D. (1994) Chemical shifts as a tool for structure determination, *Methods Enzymol. 239*, 363−392.
67. Akke, M., Liu, J., Cavanagh, J., Erickson, H. P., and Palmer, A. G. (1998) Pervasive conformational fluctuations on microsecond time scales in a fibronectin type III domain, *Nat. Struct. Biol. 5*, 55−59.
68. Kroenke, C. D., Loria, J. P., Lee, L. K., Rance, M., and Palmer, A. G. (1998) Longitudinal and transverse ^{1}H-^{15}N dipolar/^{15}N chemical shift anisotropy relaxation interference: Unambiguous determination of rotational diffusion tensors and chemical exchange effects in biological macromolecules, *J. Am. Chem. Soc. 120*, 7905−7915.
69. Palmer, A. G. (1993) Dynamic properties of proteins from NMR spectroscopy, *Curr. Opin. Biotechnol. 4*, 385−391.
70. Halle, B., and Davidovic, M. (2003) Biomolecular hydration: From water dynamics to hydrodynamics, *Proc. Natl. Acad. Sci. U.S.A. 100*, 12135−12140.
71. Kreishman-Deitrick, M., Egile, C., Hoyt, D. W., Ford, J. J., Li, R., and Rosen, M. K. (2003) NMR analysis of methyl groups at 100−500 kDa: Model systems and Arp2/3 complex, *Biochemistry 42*, 8579−8586.
72. Bocharov, E. V., Sobol, A. G., Pavlov, K. V., Korzhnev, D. M., Jaravine, V. A., Gudkov, A. T., and Arseniev, A. S. (2004) From structure and dynamics of protein L7/L12 to molecular switching in ribosome, *J. Biol. Chem. 279*, 17697−17706.
73. Goodman, J. L., Pagel, M. D., and Stone, M. J. (2000) Relationships between protein structure and dynamics from a database of NMR-derived backbone order parameters, *J. Mol. Biol. 295*, 963−978.
74. Leijonmarck, M., Eriksson, S., and Liljas, A. (1980) Crystal structure of a ribosomal component at 2.6 Å resolution, *Nature 286*, 824−826.
75. Wahl, M. C., Bourenkov, G. P., Bartunik, H. D., and Huber, R. (2000) Flexibility, conformational diversity and two dimerization modes in complexes of ribosomal protein L12, *EMBO J. 19*, 174−186.
76. Kothe, U., Wieden, H. J., Mohr, D., and Rodnina, M. V. (2004) Interaction of helix D of elongation factor Tu with helices 4 and 5 of protein L7/12 on the ribosome, *J. Mol. Biol. 336*, 1011−1021.
77. Helgstrand, M., Mandava, C. S., Mulder, F. A., Liljas, A., Sanyal, S., and Akke, M. (2007) The Ribosomal Stalk Binds to Translation Factors IF2, EF-Tu, EF-G and RF3 via a Conserved Region of the L12 C-terminal Domain, *J. Mol. Biol. 365*, 468−479.
78. Cowgill, C. A., Nichols, B. G., Kenny, J. W., Butler, P., Bradbury, E. M., and Traut, R. R. (1984) Mobile domains in ribosomes revealed by proton nuclear magnetic resonance, *J. Biol. Chem. 259*, 15257−15263.
79. Bushuev, V. N., Gudkov, A. T., Liljas, A., and Sepetov, N. F. (1989) The flexible region of protein L12 from bacterial ribosomes studied by proton nuclear magnetic resonance, *J. Biol. Chem. 264*, 4498−4505.
80. Oleinikov, A. V., Perroud, B., Wang, B., and Traut, R. R. (1993) Structural and functional domains of *Escherichia coli* ribosomal protein L7/L12. The hinge region is required for activity, *J. Biol. Chem. 268*, 917−922.
81. Mulder, F. A., Bouakaz, L., Lundell, A., Venkataramana, M., Liljas, A., Akke, M., and Sanyal, S. (2004) Conformation and dynamics of ribosomal stalk protein L12 in solution and on the ribosome, *Biochemistry 43*, 5930−5936.
82. Konarev, P. V., Petoukhov, M. V., and Svergun, D. I. (2001) MASSHA: A graphic system for rigid body modelling of macromolecular complexes against solution scattering data, *J. Appl. Crystallogr. 34*, 527−532.

BI0616450